Italian Association of Aeronautics and Astronautics
XXV International Congress
9-12 September 2019 | Rome, Italy

# SPACE-BASED DETECTION OF ORBITING OBJECTS BY USING STAR SENSORS

F. Curti[1*], V. Schiattarella [1], D. Spiller [1], D. Luchena[2],
C. Facchinetti[3], L. Ansalone[3], A. Tuozzi[3]

[1]School of Aerospace Engineering, Sapienza University of Rome,
Via Salaria 851, 00138 Rome -Italy

[2]ARCA Dynamics, Via L. di Monreale 8, 00152 Rome – Italy

[3]Italian Space Agency (ASI), Via del Politecnico snc, 00133 Rome – Italy

* Emails: fabio.curti@uniroma1.it, vincenzo.schiattarella@uniroma1.it, dario.spiller@uniroma1.it, daniele@arcadynamics.com, claudia.facchinetti@asi.it, luigi.ansalone@asi.it , alberto.tuozzi@asi.it

## ABSTRACT

*The increasing number of space activities has led to the growth of the population of resident space objects, i.e. satellites and space debris. The availability of a complete catalogue of orbiting objects is therefore extremely useful for the collision probability evaluation of present and future missions. The existing catalogues are essentially based on-ground radars, or optical measurements. The main limitation of this approach is related to the distance between the observer and the orbiting object. Such limitation can be solved by using space-based measurements. Within the framework of this application, the paper proposes the use of star sensors as orbiting observers, profiting from their disseminated optical sensors. In fact, the star sensors are typically mounted on-board of satellites for the attitude determination. The proposed approach provides the opportunity of using them for objects' detection, thus minimizing the impact in terms of cost and system architecture with respect to dedicated space object observer missions. Usually, star sensors discard information of observed moving objects against the fixed stars, losing many data that could be very useful for the Space Situational Awareness. An orbiting observer of spacecraft and space debris provides the opportunity of continuous operations with the detection of close objects within a range of a few thousands of kilometres. A star sensor in sun-synchronous orbit can observe hundreds or thousands of objects, especially in the regions over the poles.*

*This work presents a preliminary study of the Italian Space Agency project SPOT (Star sensor image on-board Processing for Orbiting objects deTection). The paper focuses on the analysis in using star sensors in LEO to detect space debris. A mission with Multi-Head Star Sensors, could have a star sensor not used for the attitude determination. The idea is to exploit this star sensor to detect moving objects, which appear as streaks in the acquired image. The main factors which affect the visibility have been considered: the sensor characteristics (sensitivity, field of view, exposure time, and boresight direction), the optical properties of the observed objects, the environment influence, and the relative velocity between target and observer. The paper shows the results by selecting up to 12 satellites in LEO as simultaneous observers.*

**Keywords:** Star sensor, Orbiting objects' detection, Space Situational Awareness.

# 1 INTRODUCTION

In space applications, the information about the location of the resident space objects (RSOs) such as satellites, space junk, and other orbital objects is critical [1], [2], [3]. It is used to periodically observe and exactly track the space objects [4],[5]. Since the location and trajectory of the space objects (specifically satellites) change, they have to be observed repeatedly in different intervals of time [6][7][8]. Space debris, defined as the remains of spacecraft and rockets, pose a growing threat to LEO, MEO and GEO space infrastructure and operations due to the large uncertainty of their population, trajectories, mass, size, etc. Any collision event with a several-millimeter sized object traveling at orbital velocity may cause irreversible damage and further avalanche multiplication of debris. The known number of space debris has increased substantially over the last decades and it is expected to grow further at a nearly exponential rate due to increased human activities in space in the 21$^{st}$ century. The tracking of space debris would allow to reduce the possibilities of having potential hazardous collisions.

The availability of a complete catalogue of orbiting objects is, therefore, extremely useful for the reliability and safety evaluation of present and future missions. The existing catalogues essentially derives from ground-based observations (optical and/or radar).

Optical observations have two mayor limitations: their period (especially in LEO) and the requirement of clear, dark skies. In fact, space objects can be detected by a telescope when they are sunlit while the sky background is dark. Optical telescopes are used for more distant orbital regions such as the geostationary ring [9] [10].

Radar observations are primarily used for the characterization of the space debris population in LEO between 200 and 2000 km [11], as this is the most practical way of studying the space debris environment as far as observable objects are larger than 1 cm [12]. Compared with the optical measurements, radars can grant a 24-hour a day observation independent from meteorological conditions and with very high sensitivity. However, above several thousand km of altitude the required radar power is too high to allow the monitoring of small space debris. Therefore, optical sensors are used in these scenarios.

Many organizations such as Defense R&D Canada, China's Shanghai Observatory and USAF, developed their ground-based stations using telescopes to observe and track satellites [9][10] [11][12].

Nowadays, the orbits of all the unclassified spacecraft and space debris are collected by AFSPC and NORAD in the TLE catalogue and are updated thanks to the observations performed by a network of 25 sensors, both radars and optical, called Space Surveillance Network (SSN). SSN processes data coming from about 80,000 observations each day.

Debris smaller than 2 mm cannot be detected by any ground-based observations even though such tiny debris may lead to the end of a spacecraft's mission. Therefore, space-based observations should be conducted to understand the environment of sub-millimeter-size debris for all the orbits.

Space-based observations are performed on-board space platforms in orbit; thus, objects can be detected more than once a day and from different and/or optimal points of view determined from the phase angle. Furthermore, there are no restrictions by weather, atmosphere and day/night cycle meaning a high operational robustness.

In this framework, ESA is developing a project, called "Optical In-Situ Monitor" [13], whose aim is to detect space debris by means of a dedicated optical telescope mounted on-board a spacecraft (which is in a sun-synchronous orbit near the terminator plane).

This paper describes a new approach to space-based detection of resident space objects using star sensor (SPOT). Unlike the ESA project, SPOT aims to detect orbiting objects by using star sensors, usually required for accurate attitude determination purposes.

SPOT will exploit data from the optical sensors already mounted on-board the spacecraft in order to minimize any impact on the main purposes of the mission. This will lead to a better knowledge of catalogued objects and the detection of new objects.
The paper is organized as follows.
In Sec. 2 some brief notions related to SPOT architecture are described.
In Sec. 3 the mathematical model required to perform the simulation is explained.
In Sec. 4 the adopted simulation environment is reported.
In Sec. 5 simulations results are shown, and in Sec. 6 conclusions and final remarks are reported.

## 2 SPOT ARCHITECTURE

The detection of orbiting objects uses the acquisition of optical measurements obtained by the star sensor. In a stabilized satellite, i.e., with a fixed attitude, stars appear as groups of pixels with a fixed position in successive images (except for movement due to noise). On the other hand, an orbiting object, that falls within the sensor's field of view (FOV), appears as an extended source spread over one or more pixels (with swiping effect), depending on its size and velocity (in terms of direction and space travelled) with respect to that of the sensor.
SPOT is set up in its nominal mode to operate by receiving information from the satellite's attitude navigation and guidance system, if the attitude conditions on angular velocity fulfil some threshold limits. In fact, the risk is to not be able to distinguish the orbiting object and the fixed star. In this configuration during the image analysis process, SPOT can recognize the stars and exclude them by applying filtering based on techniques very similar to those used during usual star tracking operations.
SPOT proposes to process the flow of data entering the system by using one or more algorithms capable of detecting moving objects.
SPOT deals with two different software modules: ON-BOARD SPOT module, for on-board data processing, and GROUND SPOT module, for ground-based data processing

### 2.1 On-board SPOT

The information required by the on-board processing of SPOT is the coordinates of the above-threshold pixels and their energy supplied as a data stream from the star sensor. The input to the system is guaranteed regardless of the type of technology used for the detector (CCD or CMOS) or for the acquisition method (rolling shutter or global shutter). For instance, the detector information of CMOS sensors is acquired line by line by the on-board data management system. For each row, consecutive pixels with sufficiently high signals are collected in segments. This pre-processing, called segmentation, is based on the comparison of the signal of each individual pixel with the average signal of its local neighborhood. Therefore, only segment information is considered for further analysis related to the detection of bodies and debris in orbit. Segmentation pre-processing data is collected with an RLE algorithm to minimize the amount of memory required.
The major critical issue of on-board processing lies in the recognition of recurring streaks belonging to the same star and consequently in the recognition of groups of pixels belonging to the same orbiting object, as known from the use of star trackers as stellar gyroscopes [14][15]. In order to do this, the following procedure, divided into three steps (with the generation of the same number of products), is applied on board:

- Clustering: this operation is performed on a single image. The segments belonging to the same object are unified in a cluster (group of pixels) that can be used to extrapolate information on the moving object.
- Fusion: this operation is necessary to recognize the persistence of an object in successive images. The fusion operation is applied to two consecutive images and allows the software to understand the direction of the moving object within the sensor area.

- Detection: moving objects are represented by streaks in the image. The processing identifies the coordinates and the acquisition epoch of the Extremal Points (EPs) of each series.

### 2.2 Ground SPOT

This block manages and processes the data sent to the ground station: the input is the output data from ON-BOARD SPOT, which is processed and collected in a database. The database will allow expert users to further process data for Space Surveillance and Tracking (SST) purposes, such as orbit determination and dimensions estimation of the detected objects.

## 3 MATHEMATICAL MODEL

A detailed visibility study has been performed to validate performances and potentialities of SPOT. All the following mathematical relationships have been taken from [16][17][18][19]. In particular, the visibility criteria of a target have been identified in relation to its magnitude, its position with respect to the observer, and the optical characteristics of the target and the sensor.

### 3.1 Magnitude evaluation

A satellite can drastically change its magnitude value, passing from a condition of visibility to one of non-visibility only due to attitude maneuvers or due to changes in kinematic orbital conditions. The relationship between the standard magnitudes $M_{std}$ (the one catalogues in the NORAD database) and the visual magnitude $M_v$ can be obtained through the relation

$$M_v = M_{std} - 15.75 + \log_{10}\left(\frac{\rho^2}{f_{ill}}\right), \tag{1}$$

where $\rho$ is the distance between observer and target and $f_{ill}$ is the illuminated fraction of the satellite (its value can range from 0 to 1). In particular, $f_{ill} = 1$ if the target is completely illuminated, $f_{ill} = 0$ if the target is not visible.
For those objects for which $M_{std}$ is unknown but the dimension is known, $M_v$ can be estimated by using the transversal section area (intended to be the minimum exposed area).

$$M_v = -26.7 - 2.5\log_{10}\big(\mu A F(\Phi)\big) + 5\log_{10}\rho\,, \tag{2}$$

where $A$ is the transversal section area, $\mu$ is the reflection coefficient ($\mu$ has been set constant and equal to 0.11 according to the literature), $\Phi$ is the phase angle (the angle between Sun-target-observer) and $F(\Phi)$ is a function which depends on the shape and attitude of the observed object.

#### 3.1.1 *Spherical objects*

Considering spherical objects with diffusive optical properties, the explicit expression for $F(\Phi)$ is

$$F(\Phi) = \frac{2}{3\pi^2}[(\pi - \Phi)\cos(\Phi) + \sin(\Phi)] \tag{3}$$

Supposing that the maximum instrumental magnitude visible from the star sensor is equal to 5.5, Table 1 shows which kind of objects is possible to detect at a given relative distance and phase angle.

| | | Relative distances (km) | | | |
|---|---|---|---|---|---|
| Diameter (cm) | Area (cm$^2$) | $\Phi = 0°$ | $\Phi = 45°$ | $\Phi = 90°$ | $\Phi = 135°$ |
| *0.1* | *$7.8540\times10^{-3}$* | **0.3905** | **0.3394** | **0.2203** | **0.0858** |
| *1* | *$7.8540\times10^{-1}$* | **3.905** | **3.394** | **2.203** | **0.8582** |
| *5* | *$1.9635\times10^{1}$* | **19.525** | **16.970** | **11.016** | **4.291** |
| *10* | *$7.8540\times10^{1}$* | **39.050** | **33.940** | **22.032** | **8.582** |
| *50* | *$1.9635\times10^{3}$* | **195.25** | **169.70** | **110.16** | **42.91** |
| *100* | *$7.8540\times10^{3}$* | **390.50** | **339.40** | **220.32** | **85.82** |
| *500* | *$1.9635\times10^{5}$* | **1952.5** | **1697.0** | **1101.6** | **429.1** |
| *1000* | *$7.8540\times10^{5}$* | **3905.0** | **3394.0** | **2203.2** | **858.2** |

Table 1: Detectable spherical objects with magnitude 5.5

### 3.1.2 *Plates*

Considering plate objects, the explicit formula for $F$ is

$$F(\varphi_1, \varphi_2) = \frac{1}{\pi}\sin(\varphi_1)\sin(\varphi_2) \tag{4}$$

where the angle $\varphi_1$ and $\varphi_2$ are defined in Figure 1. Moreover, the angles $\varphi_1$, $\varphi_2$ and $\Phi$ are related by the following equation

$$\cos\Phi = \sin\varphi_1 \sin\varphi_2 + \cos\varphi_1 \cos\varphi_2 \cos\theta \tag{5}$$

where all the required angles are defined in Figure 1. From Eq. (4), if $\varphi_1 = 0$ deg or $\varphi_1 = 180$ deg then $F = 0$, as well as for the same values of $\varphi_2$. Moreover, the behavior of $F$ is symmetric whether, once fixed one angle, the other angle is in [0,90] deg or in [90,180] deg. Accordingly, the required distance to see plate objects with a visual magnitude up to 5.5 and different size is reported in Table 2, while both $\varphi_1$ and $\varphi_2$ are in (0,90] deg.

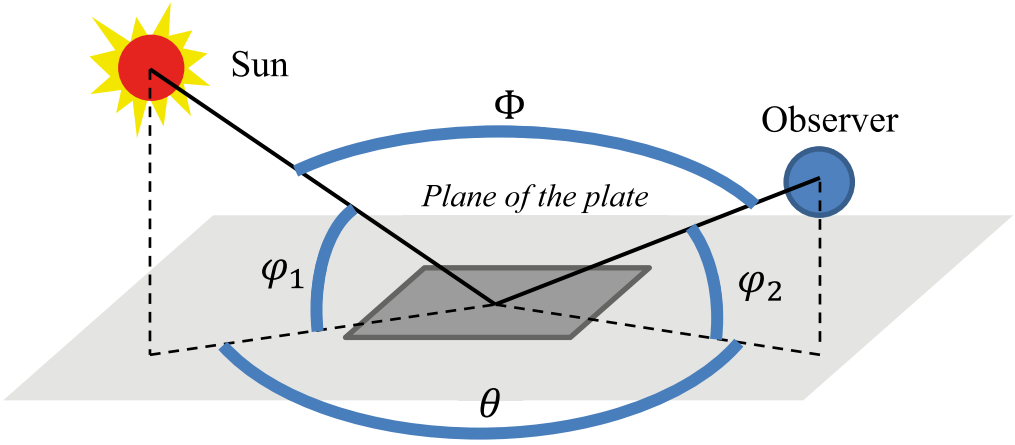


Figure 1: Definition and relationship between $\varphi_1$, $\varphi_2$, $\Phi$ and $\theta$ for the analysis of plate objects.

| | Relative distances (km) | | | | | |
|---|---|---|---|---|---|---|
| Area (cm$^2$) | $\boldsymbol{\varphi_1 = 10°}$ | | $\boldsymbol{\varphi_1 = 45°}$ | | $\boldsymbol{\varphi_1 = 90°}$ | |
| *0.01* | $\varphi_2 = 10°$ | **0.0937** | $\varphi_2 = 10°$ | **0.1891** | $\varphi_2 = 10°$ | **0.2249** |
| | $\varphi_2 = 45°$ | **0.1891** | $\varphi_2 = 45°$ | **0.3816** | $\varphi_2 = 45°$ | **0.4538** |
| | $\varphi_2 = 90°$ | **0.2249** | $\varphi_2 = 90°$ | **0.4538** | $\varphi_2 = 90°$ | **0.5397** |
| *0.25* | $\varphi_2 = 10°$ | **0.4686** | $\varphi_2 = 10°$ | **0.9455** | $\varphi_2 = 10°$ | **1.1244** |
| | $\varphi_2 = 45°$ | **0.9455** | $\varphi_2 = 45°$ | **1.9080** | $\varphi_2 = 45°$ | **2.2690** |

| | | | | | | |
|---|---|---|---|---|---|---|
| | $\varphi_2 = 90°$ | **1.1244** | $\varphi_2 = 90°$ | **2.2690** | $\varphi_2 = 90°$ | **2.6983** |
| *1* | $\varphi_2 = 10°$ | **0.9371** | $\varphi_2 = 10°$ | **1.8910** | $\varphi_2 = 10°$ | **2.2488** |
| | $\varphi_2 = 45°$ | **1.8910** | $\varphi_2 = 45°$ | **3.8160** | $\varphi_2 = 45°$ | **4.5380** |
| | $\varphi_2 = 90°$ | **2.2488** | $\varphi_2 = 90°$ | **4.5380** | $\varphi_2 = 90°$ | **5.3966** |
| *25* | $\varphi_2 = 10°$ | **4.6856** | $\varphi_2 = 10°$ | **9.4552** | $\varphi_2 = 10°$ | **11.2441** |
| | $\varphi_2 = 45°$ | **9.4552** | $\varphi_2 = 45°$ | **19.0799** | $\varphi_2 = 45°$ | **22.6900** |
| | $\varphi_2 = 90°$ | **11.2441** | $\varphi_2 = 90°$ | **22.6900** | $\varphi_2 = 90°$ | **26.9831** |
| *100* | $\varphi_2 = 10°$ | **9.3711** | $\varphi_2 = 10°$ | **18.9103** | $\varphi_2 = 10°$ | **22.4883** |
| | $\varphi_2 = 45°$ | **18.9103** | $\varphi_2 = 45°$ | **38.1598** | $\varphi_2 = 45°$ | **45.3799** |
| | $\varphi_2 = 90°$ | **22.4883** | $\varphi_2 = 90°$ | **45.3799** | $\varphi_2 = 90°$ | **53.9661** |
| *2500* | $\varphi_2 = 10°$ | **46.8556** | $\varphi_2 = 10°$ | **94.5516** | $\varphi_2 = 10°$ | **112.4415** |
| | $\varphi_2 = 45°$ | **94.5516** | $\varphi_2 = 45°$ | **190.7991** | $\varphi_2 = 45°$ | **226.8997** |
| | $\varphi_2 = 90°$ | **112.4415** | $\varphi_2 = 90°$ | **226.8997** | $\varphi_2 = 90°$ | **269.8307** |
| *$10^4$* | $\varphi_2 = 10°$ | **93.7112** | $\varphi_2 = 10°$ | **189.1033** | $\varphi_2 = 10°$ | **224.8829** |
| | $\varphi_2 = 45°$ | **189.1033** | $\varphi_2 = 45°$ | **381.5983** | $\varphi_2 = 45°$ | **453.7994** |
| | $\varphi_2 = 90°$ | **224.8829** | $\varphi_2 = 90°$ | **453.7994** | $\varphi_2 = 90°$ | **539.6615** |
| *$25\times10^4$* | $\varphi_2 = 10°$ | **$0.4686\times10^3$** | $\varphi_2 = 10°$ | **$0.9455\times10^3$** | $\varphi_2 = 10°$ | **$1.1244\times10^3$** |
| | $\varphi_2 = 45°$ | **$0.9455\times10^3$** | $\varphi_2 = 45°$ | **$1.9080\times10^3$** | $\varphi_2 = 45°$ | **$2.2690\times10^3$** |
| | $\varphi_2 = 90°$ | **$1.1244\times10^3$** | $\varphi_2 = 90°$ | **$2.2690\times10^3$** | $\varphi_2 = 90°$ | **$2.6983\times10^3$** |
| *$10^6$* | $\varphi_2 = 10°$ | **$0.4686\times10^3$** | $\varphi_2 = 10°$ | **$1.8910\times10^3$** | $\varphi_2 = 10°$ | **$2.2488\times10^3$** |
| | $\varphi_2 = 45°$ | **$0.9455\times10^3$** | $\varphi_2 = 45°$ | **$3.8160\times10^3$** | $\varphi_2 = 45°$ | **$4.5380\times10^3$** |
| | $\varphi_2 = 90°$ | **$1.1244\times10^3$** | $\varphi_2 = 90°$ | **$4.5380\times10^3$** | $\varphi_2 = 90°$ | **$5.3966\times10^3$** |

Table 2: Detectable plate objects with magnitude 5.5 and $\varphi_1 \neq 0, \varphi_2 \neq 0$.

Note that the plate model gives results very similar to the sphere one, i.e. the required distances for visibility are comparable for the two models. Thus, without loss of generality, the model of the sphere will be adopted for the simulation.

### 3.2 Dynamic condition analysis

RSOs can move in the focal plane due to

1) non-negligible angular velocities of the observer, or
2) non-negligible relative velocities between observer and target.

In these cases, the RSO signal is spread over more pixels with respect to the stationary case. Consequently, the number of photoelectrons associated to a single pixel of a streak in dynamic conditions is smaller than the number of photoelectrons associated to a pixel of a spot in stationary case.
When the number of photoelectrons is too small, the star signal can be too low to pass the preprocessing operation. Indeed, regardless of the type of preprocessing, a threshold must always be introduced to distinguish meaningful pixel from background noise. Hence, with increasing velocities, the number of detected objects (stars or RSOs) usually decreases. This problem has been already investigated in different works, e.g. [20][21].
The relative velocity $\boldsymbol{V}$ of an object moving in a frame fixed with the observer is evaluated as a function of its position $\boldsymbol{P}$ in two successive time instants, i.e.

$$\boldsymbol{\Delta P} = \boldsymbol{P}(t_{k+1}) - \boldsymbol{P}(t_k) \tag{6}$$

As follows, $t_k$ and $t_{k+1}$ will be regarded as the initial and final time for the exposure of the generic star sensor frame. Hence, the exposure time of the star sensor is defined as

$$T_{expo} = t_{k+1} - t_k \,. \tag{7}$$

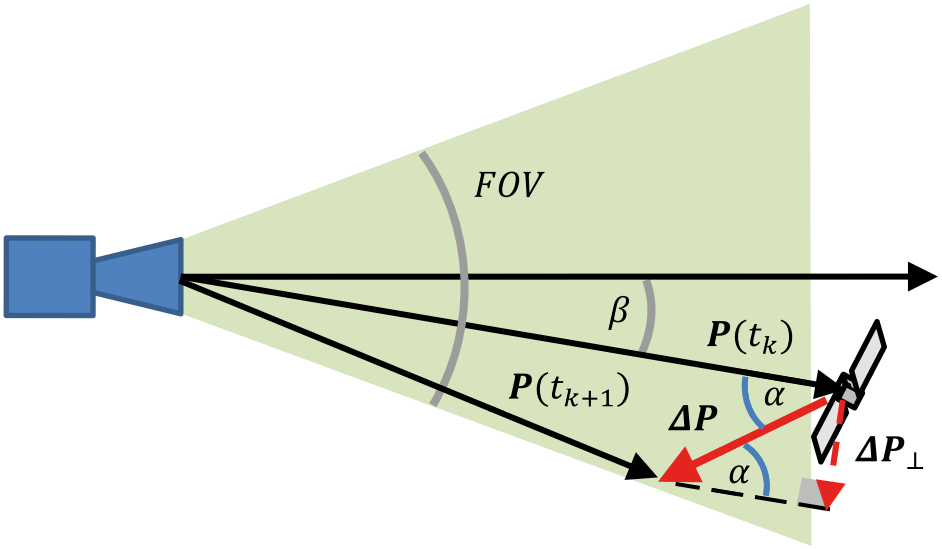


Figure 2: Object moving in the field of view of the star sensor.

When the object is within the FOV of the star sensor of the observers, the object is seen as a moving point in the focal plane if $\boldsymbol{\Delta P}$ has a non-zero orthogonal component with respect to $\boldsymbol{P}(t_k)$ (see Figure 2). Accordingly, let $\boldsymbol{\Delta P}_\perp$ be the component of $\boldsymbol{\Delta P}$ orthogonal to $\boldsymbol{P}(t_k)$ with magnitude

$$\left|\left|\boldsymbol{\Delta P}_\perp\right|\right| = \left|\left|\boldsymbol{\Delta P}\right|\right| \sin\alpha \,. \tag{8}$$

Note that, when $\boldsymbol{\Delta P}_\perp$ is equal to zero, the object appears as a stationary spot in the image and it is automatically filtered by the detection software. With reference to Figure 2, the relative displacement is related to the displacement detected into the focal plane, $\boldsymbol{v}_{FP}$, by mean of the following relation,

$$\frac{\left|\left|\boldsymbol{\Delta P}_\perp\right|\right|}{||\boldsymbol{P}(t_k)||} = \frac{||\boldsymbol{\Delta p}^*_{FP}||}{\dfrac{F+x}{\cos\beta}}, \tag{9}$$

where

$$||\boldsymbol{\Delta p}^*_{FP}|| = ||\boldsymbol{\Delta p}_{FP}|| \cos\beta \tag{10}$$

and $x$ is an unknown parameter (typically small). It is noteworthy that the term $\cos\beta$ is introduced to consider the angular displacement between the real relative velocity and the one detected into the focal plane (see Figure 3). The displacement in the focal plane is given as

$$||\boldsymbol{\Delta p}_{FP}|| = \frac{||\boldsymbol{\Delta P}_\perp||}{||\boldsymbol{P}(t_k)||} \frac{F+x}{\cos^2\beta}. \tag{11}$$

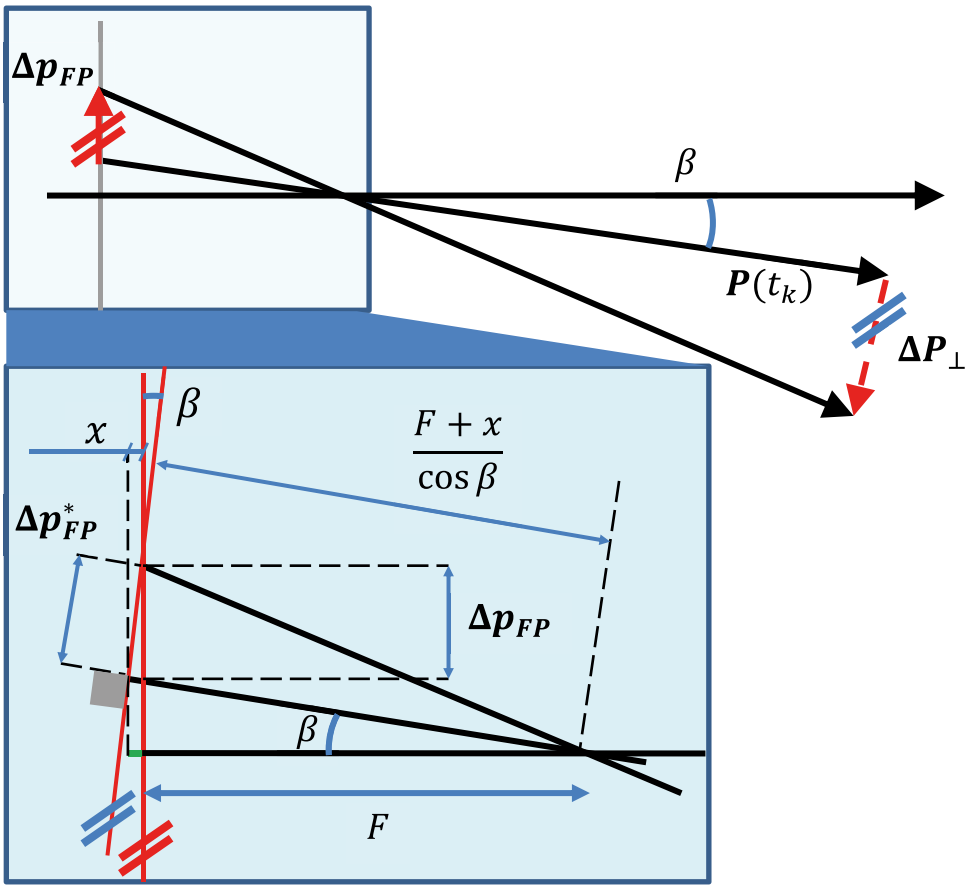


Figure 3 Detail of Figure 2.

A good feasible approximation of the previous formula is given by imposing $x = 0$, which is true when the displacement of the object is small compared to the dimension of the detector (this is true when the sampling frequency is high enough and the relative velocity is small). In this case, the displacement in the focal plane is given as

$$||\boldsymbol{\Delta p}_{FP}|| \cong \frac{||\boldsymbol{\Delta P}_\perp||}{||\boldsymbol{P}(t_k)||} \frac{F}{\cos^2\beta}. \tag{12}$$

Finally, when $\beta \cong 0$, then the estimation of $||\boldsymbol{\Delta p}_{FP}||$ can be further simplified as

$$||\boldsymbol{\Delta p}_{FP}|| \cong \frac{||\boldsymbol{\Delta P}_\perp||}{||\boldsymbol{P}(t_k)||} F. \tag{13}$$

By dividing Eq. (13) for the exposure time, the relation concerning the relative velocity and the image-plane velocity is

$$||\boldsymbol{v}_{FP}|| \cong \frac{||\boldsymbol{V}_\perp||}{||\boldsymbol{P}(t_k)||} F. \tag{14}$$

This formula can be used with good results with FOV up to 20 deg and slow objects. With reference to Figure 3, the arc-length $l$ of a moving object in the focal plane can be reasonably approximated dividing Eq. (11) by $(F + x)/\cos\beta$. Consequently, $l$ is expressed as

$$l = \frac{||\Delta \boldsymbol{p}_{FP}||}{\frac{F+x}{\cos\beta}} = \frac{||\Delta \boldsymbol{P}_{\perp}||}{||\boldsymbol{P}(t_k)||} \frac{1}{\cos\beta} \tag{15}$$

where the cosine can be reasonably ignored when the FOV is less than or equal to 20 deg. In this section, we consider a model which is very close to the one presented in [20], as well as already done in [15]. The arc length $l$ can be alternatively expressed by referring to the velocity of the object moving in the focal plane, $v_{FP}$, expressed in pixel/seconds. In this case, $l$ is expressed as

$$l = \frac{v_{FP}\, T_{expo}\, d_{pixel}}{\frac{F+x}{\cos\beta}} \cong \frac{v_{FP}\, T_{expo}\, d_{pixel}}{F} \tag{16}$$

where the last expression is the approximated evaluation. The quantity $d_{pixel}$ represents the dimension of the pixel. In stationary condition, an object with magnitude zero is associated to a signal flux intensity denoted as $G_0$, measured in $e^-/s$ and representing the number of photoelectrons emitted by a star of magnitude 0 during an exposure of one second. Considering a square detector with $n_{pixel}$ side, and the instantaneous field of view ($IFOV$) as

$$IFOV = \frac{FOV}{n_{pixel}}, \tag{17}$$

the number of covered pixels in dynamic conditions is given by

$$n_{cov} = \frac{r_{psf}\, l}{IFOV}. \tag{18}$$

In Eq. (18), $r_{psf}$ is a constant parameter related to the point spread function (PSF) of the detector. The PSF describes the response of the detector to the star signal, i.e. the spread of the star signal over several pixel.
Finally, the number of photoelectrons associated to magnitude zero star in dynamic conditions is given by

$$I_0 = \frac{G_0 T_{expo}}{n_{cov}} \tag{19}$$

and considering Eq. (18),

$$I_0 = IFOV \frac{G_0 T_{expo}}{r_{psf}\, l}. \tag{20}$$

The threshold condition for a star to be detected is that its signal $I_{th}$ is equal to $\tau_{pre}$. Hence, using the Pogson's formula

$$m_0 - m_{th} = -2.5 \log_{10} \frac{I_0}{I_{th}} \tag{21}$$

and given that $m_0 = 0$, the reference threshold magnitude can be evaluated as

$$m_{th} = 2.5 \log_{10} \frac{I_0}{I_{th}}. \tag{22}$$

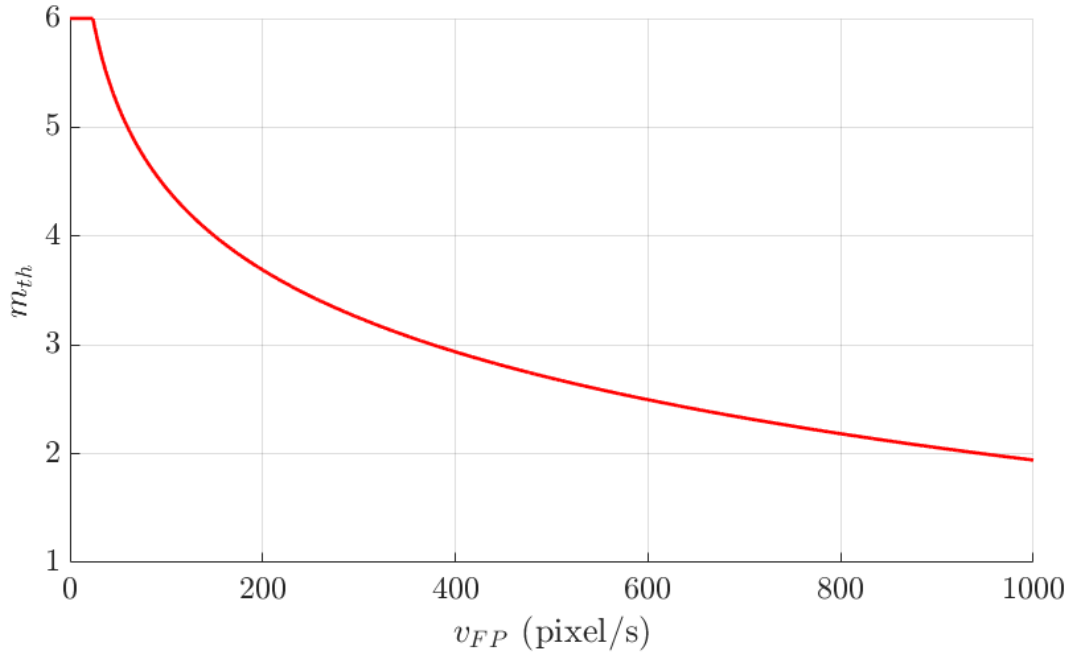


Figure 4: Magnitude threshold of moving objects

The results of this theoretical model are summarized in Figure 4. Given the object velocity in the focal plane in pixel/s, the red curve represents the maximum detectable magnitude.
Combining the results reported in Figure 4 with the analysis shown in Table 1 and Table 2, one can obtain the relationships between dimension of the object, distance from the observer and relative velocity and consequently study the detectability.

## 4 SIMULATION ENVIRONMENT

The tests are performed using satellites TLEs data and an implemented orbital propagator based on the SGP4 model described in [22]. The Simplified General Perturbations (SGP4) propagator is used with two-line mean element (TLE) sets. It considers secular and periodic variations due to Earth oblateness, solar and lunar gravitational effects, gravitational resonance effects, and orbital decay using a drag model.

### 4.1 Magnitude estimation

The evaluation of magnitude for each satellite is required to carry out the simulations. Some non-official catalogs have been used which are the result of numerous observation campaigns carried out over the years. From these catalogs, information about the standard magnitude ($M_{std}$), the three main dimensions $(x, y, z)$ and the Radar Cross-Section ($RCS$) were obtained for some of the satellites contained in the NORAD catalog.
The models described in Section 3.1 have been adopted to perform the simulation. When standard magnitude information is provided, Eq. (1) is adopted. Standard magnitude ($M_{std}$) is available for only the 23.1% of the satellites in the NORAD catalog (which contains about 18,000 TLEs). Therefore, it was necessary to obtain $M_{std}$ from other available data, making in some cases conservative assumptions.
For those objects with known dimension and unknown $M_{std}$, $M_v$ can be estimated by using Eq. (2) using the transversal section area (intended to be the minimum exposed area). Considering

conservative conditions, the transversal-section area taken from catalogued information is identified with the minimum exposed area. For the sphere, the section passing through the center has been used. Instead, for the cylinder the minor area between the circle area and the rectangular area of the lateral section has been considered. And, finally, in the case of a parallelepiped the smaller area between the sections in the three main directions has been used. In the worst case, i.e. when a specific item in the NORAD catalog does not have any available information for the estimation of its magnitude, its dimension is assigned, and magnitude is evaluated using the relationship of Eq. (2). The dimensions are assigned using a conservative approach, i.e. considering such an object as a sphere with diameter of 20 cm as reported in [23].

### 4.2 Reference systems overview

Starting from this section, the reference frame will be reported, when needed, with a subscripted appropriate symbol, while, the reference to the body (observer, target, Earth or Moon) will be reported inside superscripted brackets. To understand the following analysis and results, a brief overview of the adopted reference frame is given. Two different reference frames are adopted:

- Earth Centered Inertial (ECI) reference frame, $I = \{X_I, Y_I, Z_I\}$, with origin in the center of mass of the Earth, third axis oriented as Earth's rotational axis and first and second axes in Earth's equatorial plane to complete a right-hand Cartesian coordinate system (J2000 convention is adopted for first axis). The positions of observer and target in this reference frame are $\boldsymbol{r}_I^{(O)}$ and $\boldsymbol{r}_I^{(T)}$, respectively.
- Local-Vertical, Local-Horizontal (LVLH) reference frame, $L = \{X_L, Y_L, Z_L\}$, centered in the observer position, where $X_L$ points from the center of the Earth to the origin of $L$, $Z_L$ is perpendicular to the orbital plane and $Y_L$ completes a righthand Cartesian coordinate system. The relative distance between the observer satellite and the target is evaluated as

$$\boldsymbol{\rho} = \boldsymbol{r}^{(T)} - \boldsymbol{r}^{(O)}, \tag{23}$$

The ECI and LVLH reference frames are shown in Figure 5(a).

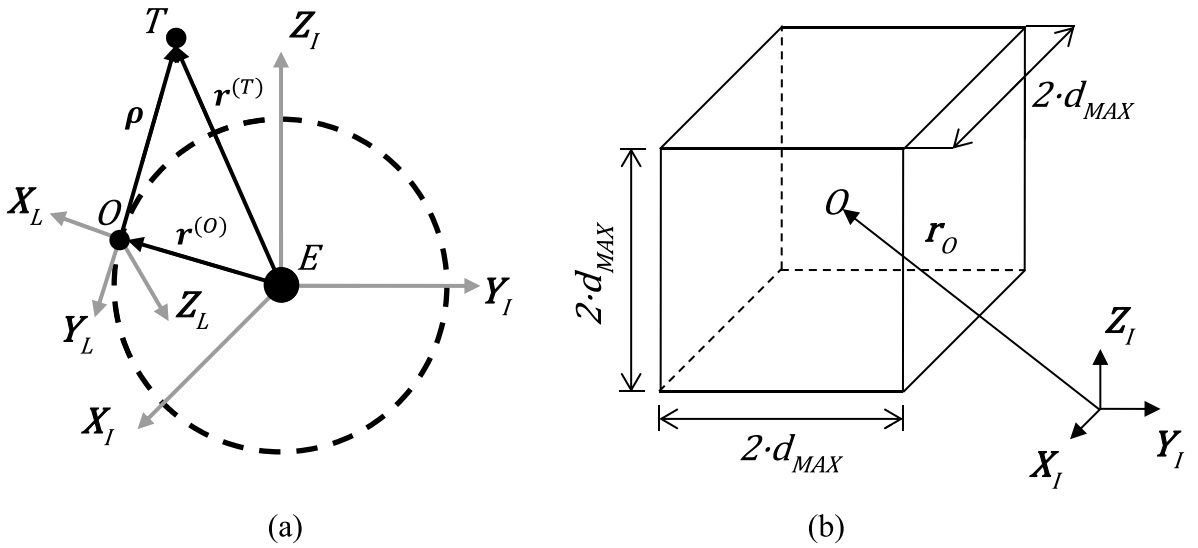


(a) (b)

Figure 5: Inertial and Local reference frames (a) and Stereographic detection box (b).

### 4.3 Visibility requirements

In this section, an analysis of the requirements for the optical detection of orbiting bodies and debris is presented. In order to detect orbiting objects with a Star Tracker, some geometrical, physical and kinematic conditions must be satisfied. In the following paragraphs, identified visibility criteria are reported.

#### 4.3.1 *Definition of the Stereographic Detection Box*

A preliminary detection condition is related to the relative distance between observer and target. With reference to Figure 5(b), the hypothesis is that the optical sensor can only see objects within a defined detection box. This condition is expressed as

$$\|\boldsymbol{\rho}\|_{\infty} \leq d_{MAX} \,. \tag{24}$$

Consequently, every satellite outside this box cannot be seen from the optical sensor (numerical results will confirm this hypothesis). For this study, it has been considered $d_{MAX} = 4000$ km (consistent with the analytical visibility analysis reported in Section 3).

#### 4.3.2 *Earth Shadow*

A major issue for optical measurements in LEO is the shadow due to the Earth exclusion cone (see Figure 6(a)). Accordingly, a consistent estimation of detected satellites must consider only satellites and/or debris that are illuminated by sunlight.

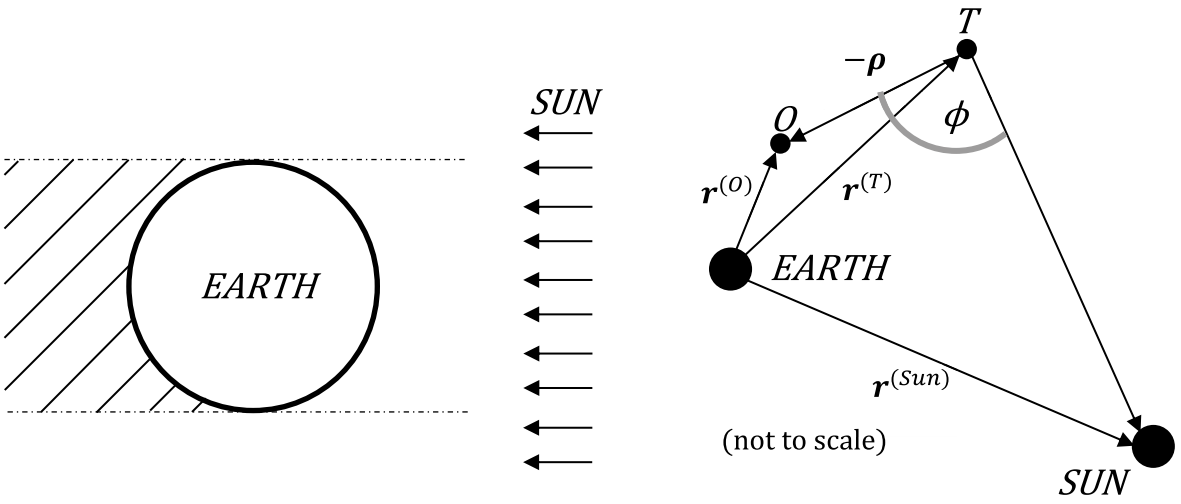


(a) (b)

Figure 6: Earth shadow (a) and phase angle from the Sun (b).

#### 4.3.3 *Phase angle from the Sun*

With reference to Figure 6(b), let $\phi$ be the phase angle defined as

$$\phi = \arccos\left(\frac{\boldsymbol{\rho} \cdot \left(\boldsymbol{r}^{(Sun)} - \boldsymbol{r}^{(T)}\right)}{\|\boldsymbol{\rho}\| \cdot \|\boldsymbol{r}^{(Sun)} - \boldsymbol{r}^{(T)}\|}\right). \tag{25}$$

An important condition for the optical detection of the target is related to the lightning condition of the target. The lightning is mainly related to the phase angle and, in order to detect a generic target, the condition $\phi \leq 135$ deg must be satisfied. When $\phi \geq 135$ deg, the observer will only

see the unlit part of the target because of the relative attitude and position, losing the visibility condition. On the contrary, when the phase angle is null, the observer will be between the Sun and the target. This is the best observation condition as the maximum illuminated surface is exposed. In further details, the expression used for $f_{ill}$ in Eq. (1) is evaluated as

$$f_{ill} = \cos\left(\frac{2}{3}\phi\right). \tag{26}$$

In this way, $f_{ill} = 1$ when $\phi = 0$, $f_{ill}$ 0.5 when $\phi = \frac{\pi}{2}$ rad = 90 deg and $f_{ill} = 0$ when $\phi = \frac{3}{4}\pi$ rad = 135 deg.

### 4.3.4 *Earth, Sun and Moon Exclusion Cone*

Bright objects within the FOV of the star tracker prevent the optical sensor to detect satellites. Hence, satellites which are within the exclusion cone of Earth, Sun or Moon cannot be considered. In fact, very bright bodies such as Sun, Moon and Earth lead to the saturation of the APS detector so that no useful information is available. The exclusion angle is evaluated as the summation of the geometric contribution, identified by $\lambda_E$, and the optical one. For the Earth, the optical contribution is mainly due to the albedo and an angle $\lambda_A = 15$ deg has been considered. As reported in Figure 7(a) the geometric contribution may be obtained as

$$\lambda_E = \arcsin\left(\frac{R_E}{\|\boldsymbol{r}^{(O)}\|}\right) \tag{27}$$

where $R_E$ is the Earth's radius.
When considering the Moon, the exclusion cone is mainly due to the optical contribution (set to 20 deg). The geometrical contribution is quite little because of the great distance between moon and observer. The Sun exclusion angle should be considered as for the Earth and the Moon. However, the condition reported in Sec. 4.3.3 is already conservative about the exclusion of the Sun inside the FOV. Accordingly, there is no need to consider the Sun exclusion angle when the phase angle condition is verified.

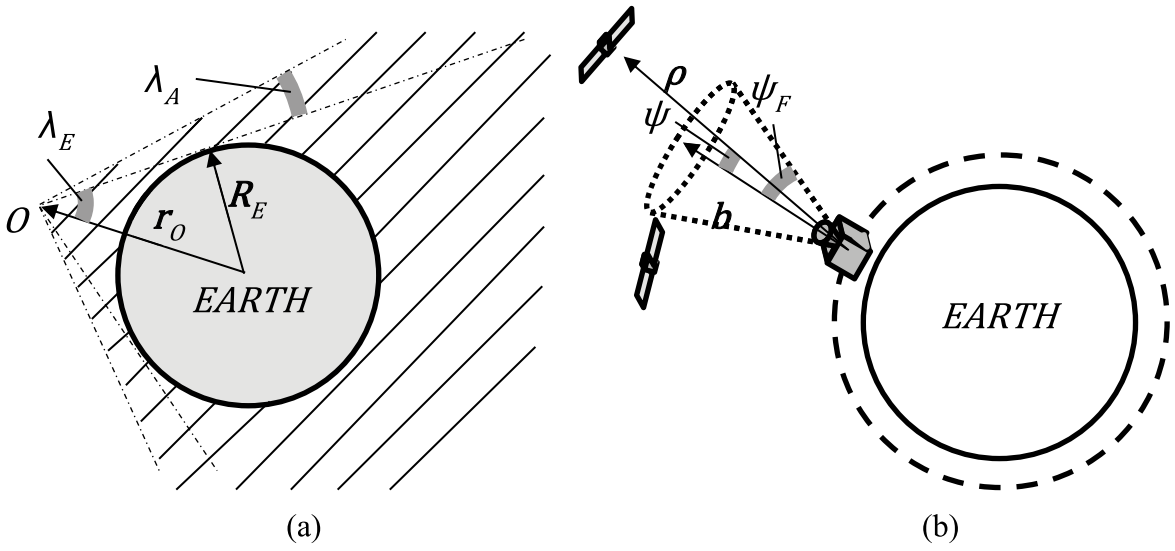


Figure 7: Earth exclusion cone (a) and star tracker field of view definition (b)

#### 4.3.5 *Star tracker Field of View*

To complete the visibility analysis, only the satellites falling within the Star Tracker FOV are considered. With reference to Figure 7(b), the selection is performed computing the angle $\psi$ between the target's position $\boldsymbol{\rho}$ and star tracker's boresight $\boldsymbol{b}$. The satellites which are separated by an angle greater than FOV semi-aperture $\psi_F$ are discarded. The angle $\psi$ is computed as

$$\psi = \arccos\left(\boldsymbol{b} \cdot \frac{\boldsymbol{\rho}}{\|\boldsymbol{\rho}\|}\right). \tag{28}$$

#### 4.3.6 *Magnitude Detection Threshold*

Satellites which magnitude is greater than the detection threshold cannot be identified. In this work, the maximum detectable magnitude is assumed to be 5.5 as it is a typical value for modern star tracker. Note that the detection threshold is a characteristic of the sensor, and it refers to instrumental magnitude. Without loss of generality, in this work the instrumental magnitude is assumed to be equal to visual magnitude to avoid the calibration issue.

#### 4.3.7 *Star tracker detection threshold in dynamic condition*

As reported in Section 3.2, the maximum detectable magnitude depends on object's relative velocity within the star tracker FOV. This relative velocity depends on boresight direction. The orbiting object will be visible if the magnitude requirement is satisfied, i.e. is less or equal to the threshold evaluated in Eq. (22).

### 4.4 Mission scenarios

The observers are simulated using the TLEs data of 12 LEO satellites:

- 4 Cosmo Skymeds (CSK1, CSK2, CSK3, CSK4)
- 5 Sentinels (S1A, S2A, S3A, S1B, S2B)
- Alos 2 (AL2)
- International space station (ISS)
- Agile (AGI).

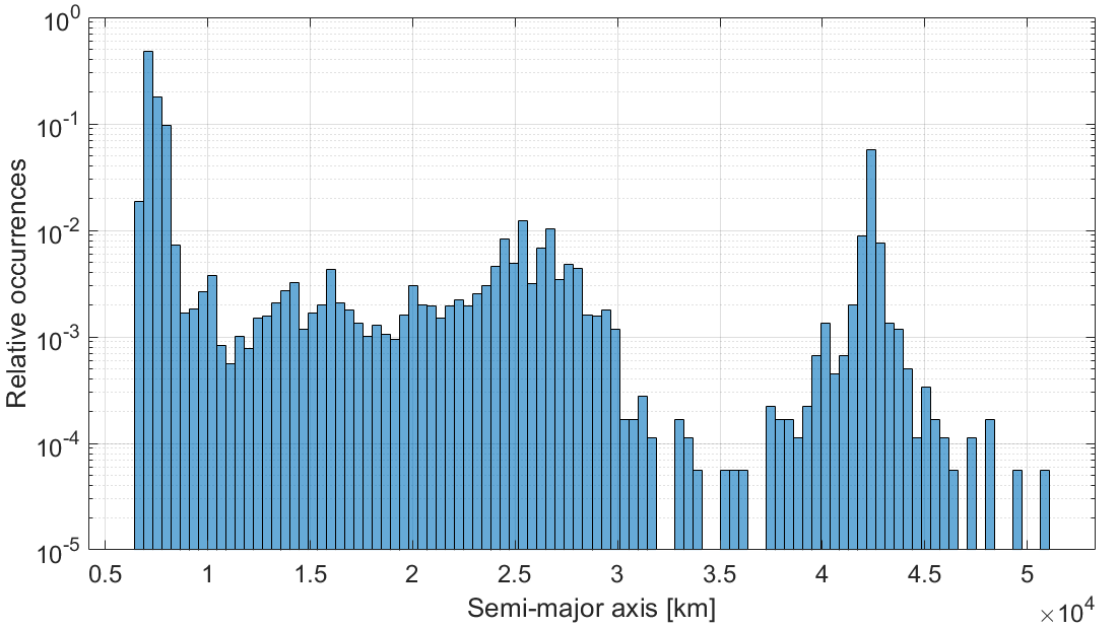


Figure 8: Distribution of NORAD cataloged objects

Figure 8 shows the distribution of space objects according to the semi-major axis. Note that the peak of the curve is for low altitude. This means that most of the space debris are in LEO. For this reason, all the 12 observers have been selected within LEO satellites.
Table 3 summarizes the main orbit's characteristics for each observer satellite.

| *Observer* | $i$ [deg] | Ω [deg] | $e$ | $\omega$ [deg] | $a$ [km] | *Boresight LVLH* |
|---|---|---|---|---|---|---|
| CSK1 | 97.8908 | 325.8719 | $1.572\cdot 10^{-4}$ | 87.9804 | $7.000675\cdot 10^{3}$ | [1, 0, 0] |
| CSK2 | 97.8912 | 325.9070 | $1.475\cdot 10^{-4}$ | 89.4346 | $7.000667\cdot 10^{3}$ | [1, 0, 0] |
| CSK3 | 97.8910 | 325.8910 | $1.436\cdot 10^{-4}$ | 91.3263 | $7.000687\cdot 10^{3}$ | [1, 0, 0] |
| CSK4 | 97.8887 | 325.8565 | $1.620\cdot 10^{-4}$ | 81.8236 | $6.999435\cdot 10^{3}$ | [1, 0, 0] |
| S1A | 98.1819 | 149.7221 | $1.338\cdot 10^{-4}$ | 79.1230 | $7.073904\cdot 10^{3}$ | [0, 1, 0] |
| S2A | 98.5672 | 217.0364 | $1.281\cdot 10^{-4}$ | 86.7912 | $7.167134\cdot 10^{3}$ | [0, 1, 0] |
| S3A | 98.6253 | 209.5706 | $1.070\cdot 10^{-4}$ | 104.6235 | $7.180796\cdot 10^{3}$ | [0, 1, 0] |
| S1B | 98.1817 | 149.5140 | $1.415\cdot 10^{-4}$ | 78.6636 | $7.073905\cdot 10^{3}$ | [0, 1, 0] |
| S2B | 98.5675 | 217.0793 | $1.153\cdot 10^{-4}$ | 80.5483 | $7.167138\cdot 10^{3}$ | [0, 1, 0] |
| AL2 | 97.9201 | 239.3900 | $1.540\cdot 10^{-4}$ | 88.6244 | $7.009145\cdot 10^{3}$ | [0, 0, 1] |
| ISS | 51.6418 | 129.4804 | $1.980\cdot 10^{-4}$ | 18.3886 | $6.786998\cdot 10^{3}$ | [0, 0, 1] |
| AGI | 2.4684 | 24.2029 | $1.197\cdot 10^{-3}$ | 162.8111 | $6.849237\cdot 10^{3}$ | [0, 0, 1] |

Table 3: Selected observers' orbits characteristics and sensor's boresight direction.

## 5 RESULTS

The simulation was performed according to a period of 1 month with a sampling time of 0.5 seconds. For each observer, the sensor's FOV dimension and boresight direction must be specified. A 20 degrees FOV star sensor is considered for every satellite.
The adopted sensor's boresight direction is different depending on the observer satellite. Considering the Local Vertical Local Horizontal frame (LVLH) the adopted boresights are:

- Along X axis for Cosmo Skymeds;
- Along Y axis for Sentinels;
- Along Z axis for Alos 2, ISS and Agile.

Observed objects are defined as the objects falling within the FOV of the sensor and satisfying the visibility requirements in Sec. 4.3 for two consecutive time instants.

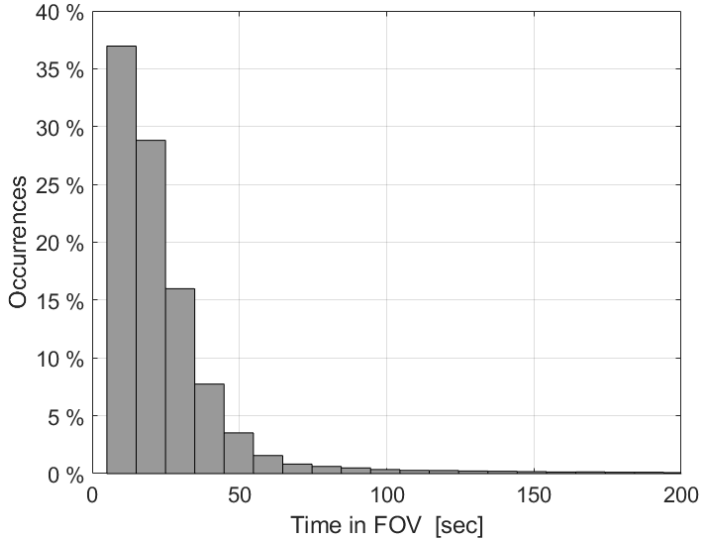


Figure 9: Distribution of elapsed time within the observers' FOVs by the observed objects

Figure 9 reports the elapsed time of the observed objects within observers' FOVs. As can be noticed, more than the 50% of the objects stands in the FOV less than 20 seconds.
Figure 10 shows the distribution of the main characteristics of observed objects.
Figure 10 (a) reports the distribution of the range distance between the observer and the targets. As can be seen, the maximum number of observed objects is given around a range of 1300 km. Results show that the number of occurrences tend to increase with the range up to this value. On the contrary, when the range increases the magnitude of the targets increases as well, reaching values beyond the detectability limit of the star sensor. Indeed, most of the detected object have magnitudes close to 5.5, as reported in Figure 10 (b) where the distribution of the estimated magnitude for the observed objects is shown.

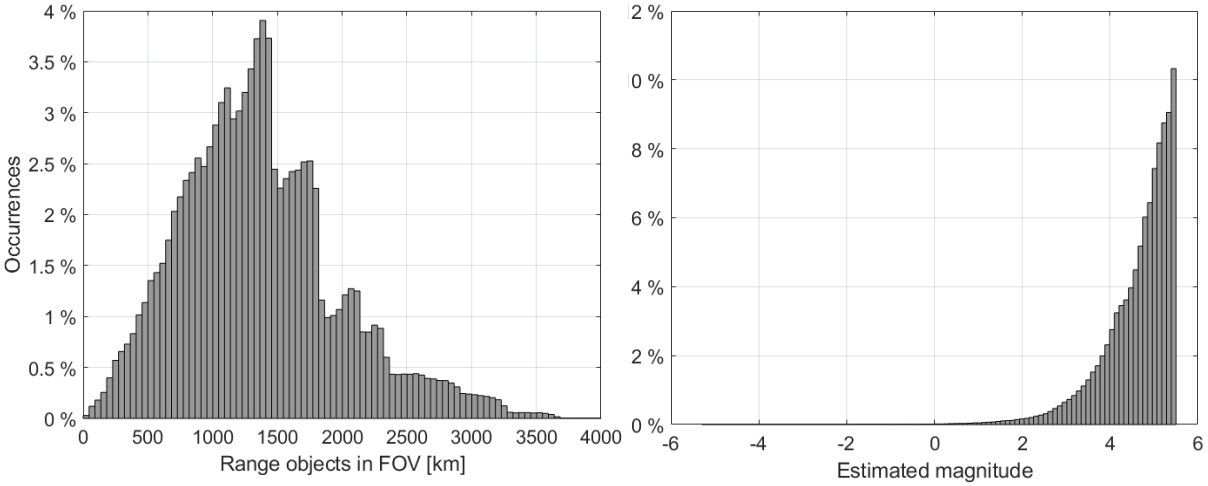


Figure 10: Observed objects main characteristics. (a) Distribution of range distance observer-targets; (b) Distribution of estimated magnitudes of the observed objects

Figure 11 reports the distribution of the estimated relative rate for the objects observed by Sentinel 1A. Similar results are obtained also for the other observers. Notice that most observed objects show less than 1 deg/s relative rates.

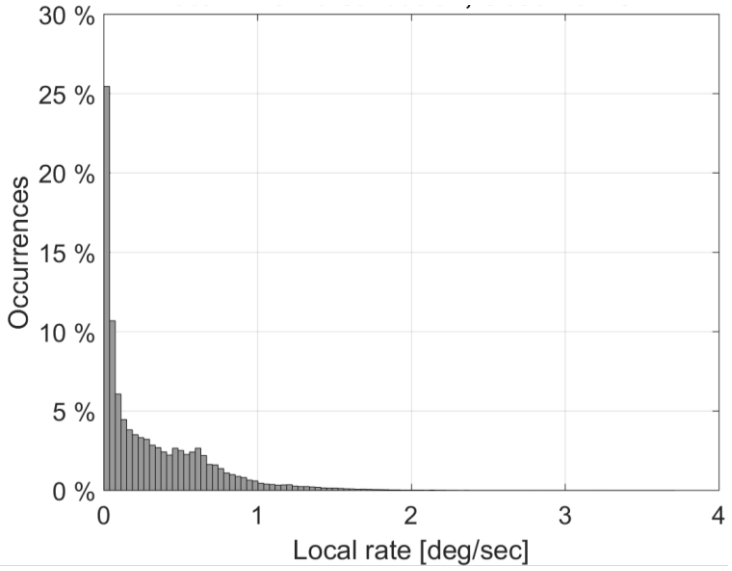


Figure 11: Distribution of estimated relative rate for objects observed by Sentinel 1A.

This result is consistent with the decreasing of star tracker detection threshold in dynamic condition. Objects with high relative rate must have a very low magnitude to be observed, i.e. they must be very close to the observer or they must have a significant section area.
Figure 12 reports the number of observed objects by a single observer (Cosmo Skymed 2) in a month. Figure 12 (a) shows the number of observed objects per day. Note that the same objects can be seen multiple times. In this case, the object is considered multiple times. As shown in the graphs, the average number of detected objects per day is about 500-600. The green bars stand for new observed objects with reference to the observed ones in the previous days. Figure 12 (b) shows the cumulative number of observed objects in a month. The total number of observed objects by a single observer is in the order of $10^4$ objects. Similar results are obtained with the other observers.

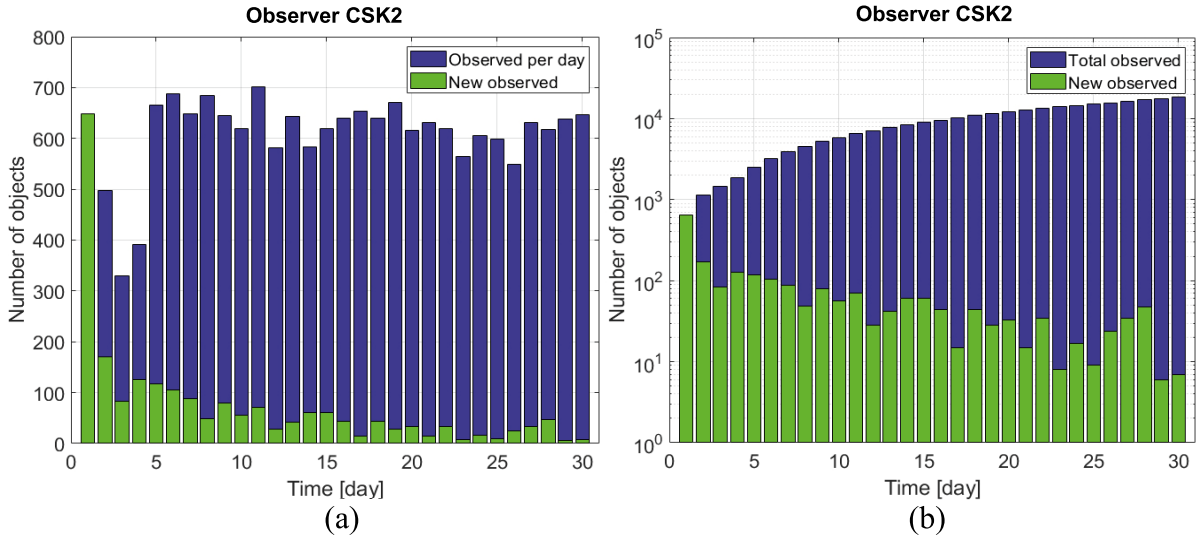


Figure 12: Observed objects by Cosmo Skymed 2 (a) Observed objects per day; (b) Cumulative number of observed objects

Figure 13 reports the cumulative number of observed objects by simultaneous observers:

- Figure 13 (a) shows the number of observed objects by Cosmo Skymed 1 and 2 in a month. The total number of observed objects by these 2 observers in a month is in the order of $10^4$ objects as for a single observer. This means that Cosmo Skymed 1 and 2 basically observe the same objects.

- Figure 13 (b) shows the number of observed objects by the four Cosmo Skymeds in a month. The total number of observed objects increases with reference to 2 observers and the same number of objects observed by only CSK1 and CSK2 is obtained in about 10 days.

- Figure 13 (c) shows the number of observed objects by the four Cosmo Skymeds and the five Sentinels in a month. The total number of observed objects increases of one order of magnitude leading to $10^5$ observed objects in a month. The reason explaining this increasing is the addition of Sentinels observers that can see different objects w.r.t the observed by Cosmo Skymed Satellite.

- Figure 13 (d) shows the number of observed objects by all the 12 selected satellites in a month. The total number of observed objects increases but not significantly.

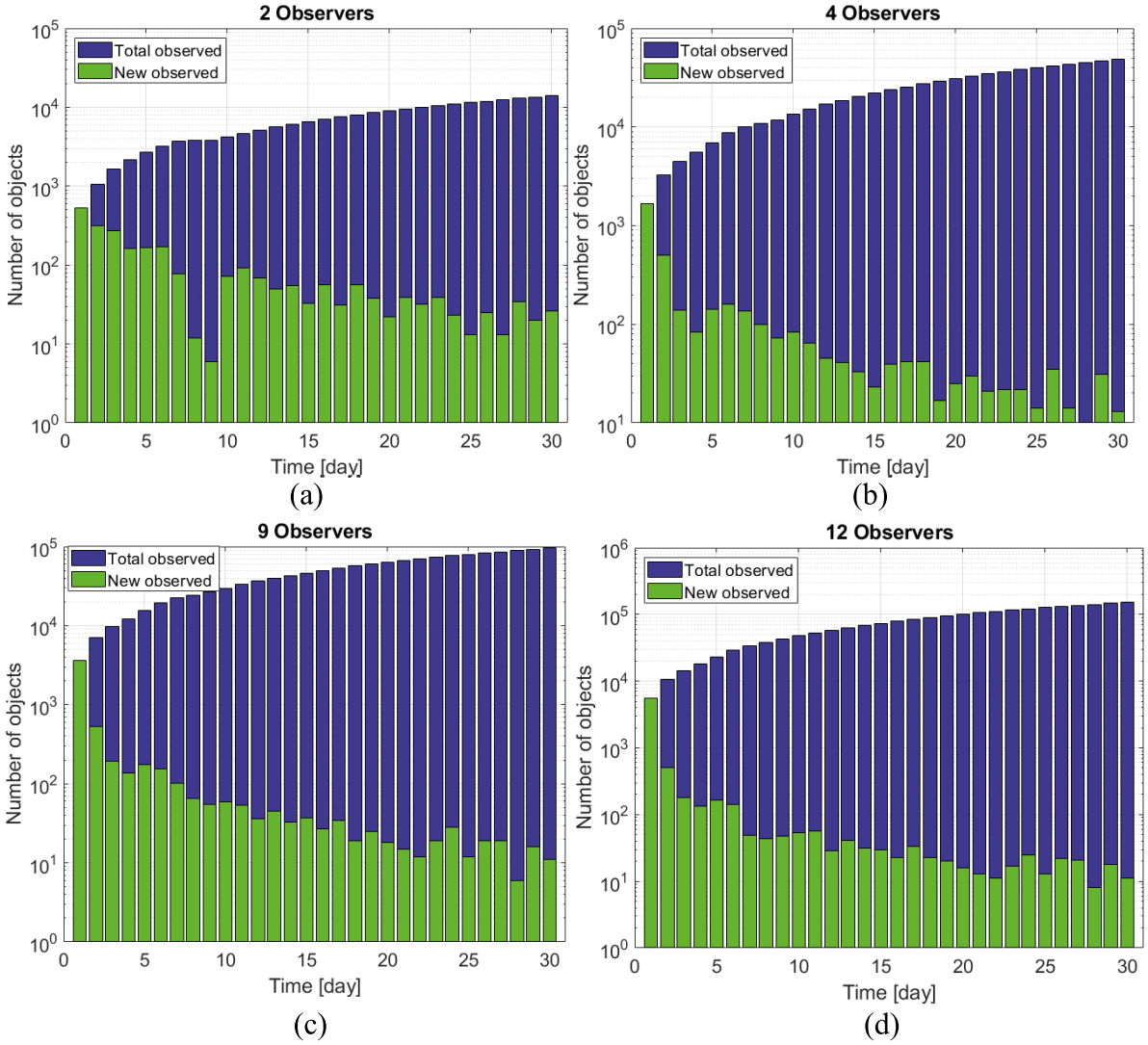


Figure 13: Number of observed objects by simultaneous observers. (a) 2 Observers: CSK1, CSK2; (b) 4 Observers: Cosmo Skymeds; (c) 9 Observers: Cosmo Skymeds and Sentinels; (d) 12 Observers.

Figure 14 shows the total number of observations in one month by every observer (blue bars). Note that an object observed multiple times is considered as a single observation.

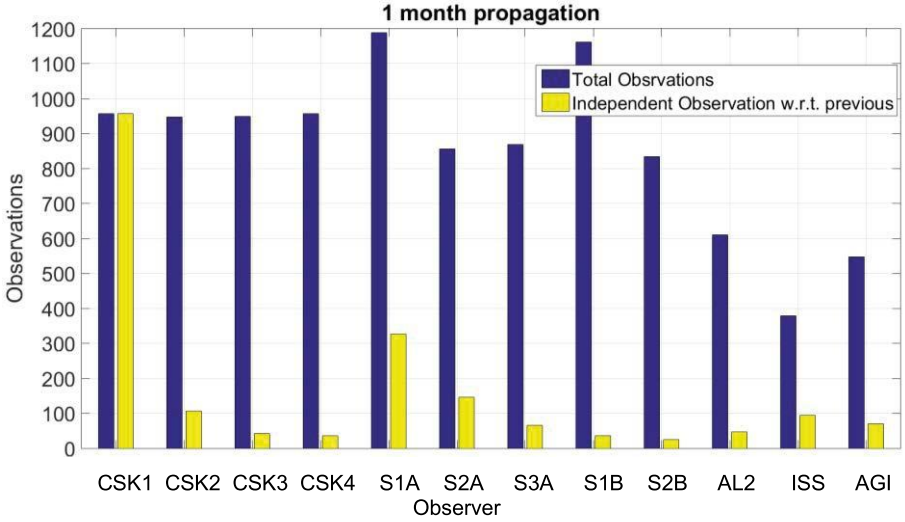


Figure 14: Total number of observations for each observer in one month.

Sentinel 1A and Sentinel 1B are the observers with the maximum number of total observations while ISS is the one with the minimum number. This depends by the adopted boresight direction and satellite's orbit (altitude and inclination). Yellow bars stand for *independent observations,* i.e. the number of different observed objects w.r.t. the observed ones by the previous observers. Obviously, for the first observer, Cosmo-Skymed 1, all the observations are independent since no other observers can be used to compare them.
Figure 15 helps to evaluate the total number of different objects seen in one month. As can be seen about 1900 different objects can be simultaneously detected by 12 observers.

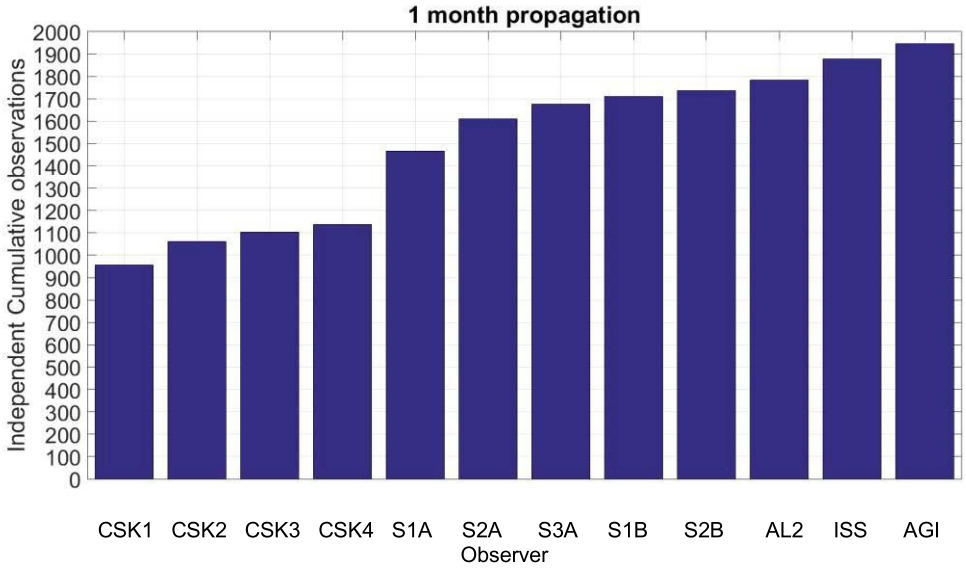


Figure 15: Independent cumulative observations by all in one month.

## 6 CONCLUDING REMARKS

The paper analyzes the opportunity of using star sensors to perform operations of space surveillance and tracking. Considering observers in LEO, each single observer can detect about 900 different objects in one month. Within this time interval, objects can be observed multiple times, reaching a total number of observed objects of about ten thousand considering repetitions. It is noteworthy that this feature can be advantageous for detection and tracking. Most of the observed objects are detected for time intervals lower than 20 seconds with magnitudes closer to the sensor's detectability limit which has been set to 5.5.
In this paper, the opportunity to adopt up to 12 simultaneous observers has been investigated, showing that, while increasing the number of observers, the number of detected objects increases as well. However, it is shown that collocated objects do not improve significantly the performances of SPOT. Using twelve observers, about two thousand different objects are detected, a hundred thousand if repetitions are considered.
In conclusion, the simulation analysis has proven the potentialities of SPOT. Future in-orbit demonstrations will be carried out to confirm the expected outcomes of this research.

## REFERENCES

[1] D. Mehrholz, L. Leushacke. Detecting, tracking and imaging space debris. *ESA Bulletin (ISSN 0376-4265)*, **109**, pp. 128-134 (2002).

[2] R. Leitch, I. Hemphil. Sapphire: A Small Satellite System for the Surveillance of Space in "Proceeding of *24th Annual AIAA/USU Conference*", Logan, UT, USA, (2010).

[3] J. C. Liou, D. Shoots. Orbital Debris Quarterly News. *NASA Orbital Debris Program Office*, **11**, (2007).

[4] L. M. Simms, et. al. Optical Payload for the STARE Mission in "Proceeding of *SPIE, Sensors and Systems for Space Applications IV*", **8044**, pp. 13 (2011).

[5] J. Kim, et. al. Visibility Analysis of Domestic Satellites on Proposed Ground Sites for Optical Surveillance. *Journal of Astronomy and Space Sciences*. **28(4)**, pp. 319-332 (2011).

[6] A. R. Vincent, et. al. Analysis of Stellar Radiance Contamination in Observed Satellite Spectra in "Proceeding of *SPIE, Ground-based and Airborne Instrumentation for Astronomy IV*", **8446**, pp. 10, (2012).

[7] T. Schildknecht. Optical surveys for space debris. *The Astronomy and Astrophysics Review*, **14**, pp. 41-111, (2007).

[8] M. A. Earl. The Space Surveillance Research and Analysis Laboratory. *Journal of the Royal Astronomical Society of Canada*, **94**, pp. 213, (2000).

[9] T. Schildknecht, R. Musci, M. Ploner, S. Preisig, J. de Leon Cruz, H. Krag. Optical observation of space debris in the geostationary ring in "Proceeding of the *Third European Conference on Space Debris*", Darmstadt, Germany, (2001).

[10] G. Tommei, A. Milani, A. Rossi. Orbit determination of space debris: admissible regions. *Celestial Mechanics and Dynamical Astronomy,* **97** pp. 289-304, (2007).

[11] D. Mehrholz. Radar observations in low earth orbit. *Advances in Space Research*, **19**, pp. 203-212 (1997).

[12] T. Sato, T. Wakayama, T. Tanaka, K.-i. Ikeda, I. Kimura. Shape of space debris as estimated from radar cross section variations. *Journal of spacecraft and rockets*, **31**, pp. 665-670. (1994).

[13] J. Utzmanna, L. Ferreirab, N. Strasserc, G. Vivesd, D. Probste, N. Lièvref. Optical In-Situ Monitor A Breadboard System to Enable Space-Based Optical Observation of Space Debris in "Proceeding *69th International Astronautical Congress (IAC)*", Bremen, Germany, (2018).

[14] F. Curti, D. Spiller, L. Ansalone, S. Becucci, D. Procopio, F. Boldrini, P. Fidanzati, G. Sechi, High angular rate determination algorithm based on star sensing in "Proceedings of *Advances in the Astronautical Sciences Guidance, Navigation and Control (AAS)*", Vail, Colorado, USA, (2015).

[15] F. Curti, D. Spiller, L. Ansalone, S. Becucci, D. Procopio, F. Boldrini, P. Fidanzati, Determining high rate angular velocity from star tracker measurements in "Proceedings of the *66th International Astronautical Congress*, Jerusalem, Israel, (2015).

[16] G. A. McCue, J. G. Williams, J. M. Morford, Optical Characteristics of Artificial Satellites in *Planet. Space Sci*. **19** pp. 851. (1971).

[17] R. H. Giese., Attitude determination from specular and diffuse reflection by cylindrical artificial satellites, *S.A.O. Special Report No.* **127**, (1963).

[18] W. E. Krag, Visible magnitude of typical satellites in synchronous orbits, *Technical Report, Massachusetts Institute of Technology*, Lexington Lincoln Laboratory, (1974).

[19] M. Hejduk, Specular and diffuse components in spherical satellite photometric modeling, in: "Proceedings of the *Advanced Maui Optical and Space Surveillance Technologies Conference"*, p. E15.

[20] C. C. Liebe, K. Gromov, and D. M. Meller, Toward a stellar gyroscope for spacecraft attitude determination, *Journal of Guidance, Control, and Dynamics*, **27**, pp. 91-99, (2004).

[21] T. Dzamba and J. Enright, Ground testing strategies for verifying the slew rate tolerance of star trackers, *Sensors*, **14**, pp. 3939-3964, (2014).

[22] D. A. Vallado, W. McClain. "Fundamentals of Astrodynamics and Applications". Microcosm Press, (2007).

[23] F. Curti, D. Spiller, V. Schiattarella, R. Orsi. Recognition of Orbiting-Objects through Optical Measurements of Light reflecting-targets by using Star-sensors in "Proceeding *1st IAA Conference on Space Situational Awareness"*, Orlando, Florida, USA, (2017).